

Carbon monoxide intensity mapping at moderate redshifts

Patrick C. Breysse,^{1*} Ely D. Kovetz,^{2 †} and Marc Kamionkowski^{1*}

¹ *Department of Physics and Astronomy, Johns Hopkins University, Baltimore, MD 21218 USA*

² *Theory Group, Department of Physics and Texas Cosmology Center, The University of Texas at Austin, Texas 78712, USA*

2 February 2019

ABSTRACT

We present a study of the feasibility of an intensity-mapping survey targeting the 115 GHz CO(1-0) rotational transition at $z \sim 3$. We consider four possible models and estimate the spatial and angular power spectra of CO fluctuations predicted by each of them. The frequency bandwidths of most proposed CO intensity mapping spectrographs are too small to use the Limber approximation to calculate the angular power spectrum, so we present an alternative method for calculating the angular power spectrum. The models we consider span two orders of magnitude in signal amplitude, so there is a significant amount of uncertainty in the theoretical predictions of this signal. We then consider a parameterized set of hypothetical spectrographs designed to measure this power spectrum and predict the signal-to-noise ratios expected under these models. With the spectrographs we consider we find that three of the four models give an SNR greater than 10 within one year of observation. We also study the effects on SNR of varying the parameters of the survey in order to demonstrate the importance of carefully considering survey parameters when planning such an experiment.

Key words: cosmology: theory – cosmology: large-scale structure of universe – cosmology: diffuse radiation

1 INTRODUCTION

Over the last decade studies of the cosmic microwave background from experiments like WMAP (Hinshaw et al. 2013) and Planck (Planck Collaboration et al. 2013) have provided unparalleled insight into the structure of the universe at the surface of last scattering. Meanwhile, large galaxy surveys such as the Sloan Digital Sky Survey (Adelman-McCarthy et al. 2008) have probed the structure of the universe at low redshifts. However, there is a large period of cosmic history for which we have very little information from direct observations. At some point, galaxies become too faint to detect individually. A relatively new technique known as intensity mapping has arisen as a way to fill this gap. First proposed by Sugimotohara, Sugimotohara, & Spergel (1999), intensity mapping involves studying the large scale fluctuations in the intensity of a given spectral line emitted by a large number of unresolved objects. Since more distant emitters will be more highly redshifted, this technique could allow the study of the three dimensional structure of the universe.

Intensity mapping can be performed using many different spectral lines. The most commonly discussed is the 21 cm neutral hydrogen line (Furlanetto, Oh, & Briggs 2006).

However, other lines trace different physical processes, and some lines may be easier to study, either because they are brighter or they appear in a less difficult frequency band. Thus it is useful to study other lines in addition to the 21 cm line. Some other lines which have been proposed include CII (Gong et al. 2012) and Ly α (Pullen, Dore, & Bock 2013b). Here we focus on the rotational transitions of carbon monoxide, particularly the lowest order transition CO(1-0) at 115 GHz. CO forms primarily in star forming regions, so intensity mapping with this line provides information on the spatial distribution of star formation in the universe. In addition, the frequencies of the CO transitions fall within a range where existing infrastructure could be adapted to studying it. CO intensity fluctuations were first studied by Righi, Hernández-Monteagudo, & Sunyaev (2008) as a foreground contaminant to CMB measurements, then later as a tracer of large scale structure (Visbal & Loeb 2010; Lidz et al. 2011; Pullen et al. 2013a).

In this paper we expand on the work of Pullen et al. (2013a) and study the feasibility of a CO intensity mapping survey targeted at $z \sim 3$. Since this is the redshift where the cosmic star formation rate is expected to be highest (Hopkins & Beacom 2006), this is a good place to attempt a first detection of this signal. Once the techniques for measuring and analyzing this signal are demonstrated successfully at this moderate redshift, surveys could be performed at redshifts corresponding to other periods, such as the epoch

* pbreysse@pha.jhu.edu (PCB); kamion@pha.jhu.edu (MK)

† elykovetz@gmail.com (EDK)

of reionization (Lidz et al. 2011; Muñoz & Furlanetto 2013). We consider four models for cosmological CO emission from the literature and estimate the strength of the CO signal predicted by each. In doing so, we demonstrate a simple one-parameter family of models which can account for a wide variety of assumptions about CO emission. When we calculate the power spectra using these models, we find that the difference in amplitude between the largest amplitude signal and the smallest is roughly two orders of magnitude, which clearly illustrates the lack of theoretical understanding of star formation physics at high redshifts. When studying the prospects for an experiment to detect this signal, we explore the effect of the instrumental parameters on the predicted signal-to-noise ratio and demonstrate the importance of carefully considering the values of these parameters when designing a survey. In particular, attempting to survey too large of an area of the sky or choosing a spectrograph with insufficient resolution can significantly decrease the chance of detecting the CO signal.

In Section 2 below we will summarize four models from the literature and use them to estimate the power spectrum of CO fluctuations. In Section 3 we will estimate the signal-to-noise ratios that would be obtained with an optimal survey under the assumptions of these models. We conclude in section 4. For all of the calculations presented below we use the following Λ CDM cosmological parameters: $(\Omega_b, \Omega_m, \Omega_\Lambda, h, \sigma_8, n_s) = (0.046, 0.27, 0.73, 0.7, 0.8, 1)$.

2 MODELING CO EMISSION

In this section we will outline our method for modeling the power spectrum of CO fluctuations.

2.1 Deriving the CO Temperature

When calculating the average CO brightness temperature, we follow the method presented by Lidz et al. (2011), which is summarized here. The specific intensity of a CO line observed at frequency ν_{obs} at $z=0$ can be found from the radiative-transfer equation,

$$I(\nu_{\text{obs}}) = \frac{c}{4\pi} \int_0^\infty \epsilon[\nu_{\text{obs}}(1+z')] \frac{dz'}{H(z')(1+z')^4}, \quad (2.1)$$

where $H(z)$ is the Hubble parameter and $\epsilon[\nu_{\text{obs}}(1+z')]$ is the proper volume emissivity of the line in question. CO is emitted from within halos, so it is natural to calculate the volume emissivity from a halo luminosity function. We use a simple estimate of the specific luminosity,

$$L_{\text{CO}} = A\delta(\nu - \nu_{\text{CO}}) \left(\frac{M}{M_\odot} \right) L_\odot, \quad (2.2)$$

which is linear in halo mass. We have assumed that the targeted line is a Dirac delta function emitted at frequency ν_{CO} . The parameter A is an overall normalization which we will calculate in section 2.1. We define a minimum mass $M_{\text{CO},\text{min}}$ below which halos are too small to emit CO lines, and we assume that a fraction f_{duty} of halos more massive than $M_{\text{CO},\text{min}}$ are emitting at any given time. For a given

halo mass function dn/dM the volume emissivity is then

$$\epsilon(\nu, z) = A\delta(\nu - \nu_{\text{CO}})(1+z)^3 f_{\text{duty}} \times \int_{M_{\text{CO},\text{min}}}^\infty M \frac{dn(z)}{dM} dM. \quad (2.3)$$

For CO lines emitted at redshift z_{CO} , this gives a specific intensity

$$I(\nu_{\text{obs}}) = \frac{A}{4\pi} \frac{1}{\nu_{\text{CO}}} \frac{c}{H(z_{\text{CO}})} f_{\text{duty}} \int_{M_{\text{CO},\text{min}}}^\infty M \frac{dn(z_{\text{CO}})}{dM} dM, \quad (2.4)$$

or, written as a brightness temperature,

$$\langle T_{\text{CO}} \rangle = \frac{A}{8\pi} \frac{1}{\nu_{\text{CO}}^3} \frac{c^3}{2k_B H(z_{\text{CO}})} f_{\text{duty}} (1+z_{\text{CO}})^2 \times \int_{M_{\text{CO},\text{min}}}^\infty M \frac{dn(z_{\text{CO}})}{dM} dM. \quad (2.5)$$

2.2 Theoretical Models

With the above expression for the average CO temperature, we now need a model of CO emission which can allow us to calculate the parameter A . In this section, we consider four such models. The first and simplest is proposed by Visbal & Loeb (2010), hereafter referred to as VL10. They estimate the star-formation rate for a halo of mass M by assuming that a fraction $f_\star = 0.1$ of the baryons in a halo form stars at a constant rate over a time period $t_s \approx 10^8$ years, where f_{duty} is the ratio of this time to the Hubble time at redshift z_{CO} . This gives a star formation rate (SFR) of

$$\text{SFR} = \frac{f_\star}{t_s} \frac{\Omega_b}{\Omega_m} M. \quad (2.6)$$

With this relation, we can determine the CO luminosity of a halo if we have a relationship between SFR and L_{CO} . In this model, this relation is obtained by measuring the ratio of CO luminosity to SFR from M82, which is observed to be $3.7 \times 10^3 L_\odot / (M_\odot/\text{yr})$ (Weiß, Walter, & Scoville 2005). Combining these scaling relations allows us to set the value of the parameter A from equation (2.2). The value in this model is

$$A_{\text{VL10}} = 6.24 \times 10^{-7}. \quad (2.7)$$

This value can be used with equation (2.5) to determine the average brightness temperature.

The second model we consider is Model A from P13. The CO luminosity function is calculated similarly to the VL10 model, but instead of using the M82 normalization, they use a set of empirical scaling relations described by Carilli (2011). They first relate CO luminosity to FIR luminosity, then FIR luminosity to SFR, and then SFR to halo mass in a similar manner to VL10. This gives a luminosity function which is still linear in mass, but with a different normalization

$$A_{\text{P13A}} = 2 \times 10^{-6}. \quad (2.8)$$

Model B from P13 uses a slightly different method to calculate the CO brightness temperature. Instead of trying to calculate a luminosity function, this model assumes that

the star formation rate S follows the Schechter function:

$$\Phi(S)dS = \phi_* \left(\frac{S}{S_*} \right) \exp\left(-\frac{S}{S_*}\right) \frac{dS}{S_*}, \quad (2.9)$$

where ϕ_* is a characteristic density and S_* is a characteristic star formation rate (Schechter 1976). Integrating this function gives the cosmic SFR density, which can then be combined with the same SFR-CO luminosity scaling relation used in model P13A to get an estimate of the CO volume emissivity. This emissivity can then be entered into equation (2.1) to get the CO brightness temperature. Though the calculation of $\langle T_{\text{CO}} \rangle$ in this model is somewhat more involved than the one described in equations (2.1)-(2.5), we can get a reasonable estimate of the brightness temperature in model P13B simply by adjusting the value of A . P13 state that $\langle T_{\text{CO}} \rangle$ in model B is roughly a factor of 4.8 higher than in model A at $z \sim 3$, so the brightness temperature in model P13B can be calculated using equations (2.1)-(2.5) with

$$A_{\text{P13B}} = 9.6 \times 10^{-6}. \quad (2.10)$$

The final model we look at here is proposed by Righi, Hernández-Montegudo, & Sunyaev (2008), which we will refer to as R08. Instead of just assuming that some fraction of halos are forming stars at any given time, the R08 model assumes that star forming episodes happen following major merger events. They estimate that the mass M_* of stars formed when two halos of mass M_1 and M_2 merge into a halo of mass M is

$$M_* = 4 \frac{\Omega_b}{\Omega_m} f_* \frac{M_1 M_2}{M}. \quad (2.11)$$

From there, one can calculate the merger rates for halos of a given mass and integrate over all possible masses to determine the total star formation rate. The authors then use the same M82 normalization from the VL10 model to calculate the CO luminosity. As with model P13B, the full calculation of $\langle T_{\text{CO}} \rangle$ in R08 is more complicated than what we have shown here thus far, but we can obtain a good approximation of their result by choosing the correct value for A . In this case the necessary value is approximately twice the one used for model P13A

$$A_{\text{R08}} = 4 \times 10^{-6}. \quad (2.12)$$

The expression for CO brightness temperature from equation (2.5) can be rewritten as

$$\langle T_{\text{CO}} \rangle(z) = -0.60 \left[\frac{A}{2 \times 10^{-6}} \right] \left[\frac{2.2 \times 10^9 \text{ yr}}{t_H} \right] \left[\frac{H(z=3)}{H(z)} \right] \times \left[\frac{1+z}{4} \right]^2 \left[\frac{\int_{M_{\text{CO},\text{min}}}^{\infty} M \frac{dn}{dM} dM}{7.05 \times 10^9 M_{\odot}/\text{Mpc}^3} \right], \quad (2.13)$$

where the numerical values are given for model P13A targeted at $z = 3$ a minimum halo mass of $M_{\text{CO},\text{min}} = 10^9 M_{\odot}$. Table 1 gives the fiducial values of $\langle T_{\text{CO}} \rangle$ for the four models above. It is clear that there is a large amount of theoretical uncertainty regarding the amplitude of the expected CO signal. This justifies our decision to simplify our estimation of $\langle T_{\text{CO}} \rangle$ in models P13B and R08, since the differences between our calculations and the full calculations will be considerably smaller than the differences between the models. For the remainder of this paper we will consider only model P13A at $z = 3$ unless stated otherwise. However, the reader should bear in mind the broad range of theoretical possibilities when following the rest of our results.

Table 1. Fiducial $\langle T_{\text{CO}} \rangle$ values at redshift 3 for each of the four models we consider.

Model	$\langle T_{\text{CO}} \rangle$ (μK)
VL10	0.19
P13A	0.60
R08	1.20
P13B	2.88

2.3 The CO Power Spectrum

A simple way to estimate the power spectrum of CO emission is given in Lidz et al. (2011). For a given $\langle T_{\text{CO}} \rangle$, the three dimensional power spectrum should take the form

$$P_{\text{CO}}(k, z) = \langle T_{\text{CO}} \rangle^2(z) [b^2(z)P_m(k, z) + P_{\text{shot}}(z)]. \quad (2.14)$$

The first term gives the contribution of the power spectrum from the clustering of matter in the Universe. Since CO is emitted from within halos, this term is simply the halo power spectrum scaled by $\langle T_{\text{CO}} \rangle$. The halo power spectrum is calculated by multiplying the linear power spectrum $P_m(k, z)$ by a mass-averaged bias factor

$$b(z) = \frac{\int_{M_{\text{CO},\text{min}}}^{\infty} M \frac{dn}{dM} b(M, z) dM}{\int_{M_{\text{CO},\text{min}}}^{\infty} M \frac{dn}{dM} dM}. \quad (2.15)$$

For the mass-dependent bias, $b(M, z)$, we use

$$b(M, z) = 1 + \frac{\nu(M, z) - 1}{\delta_c}, \quad (2.16)$$

where $\delta_c = 1.69$, $\nu(M, z) = \delta_c / \sigma(M, z)$, and $\sigma(M, z)$ is the RMS density fluctuation in a spherical region containing mass M (Mo & White 2002). The second term of equation (2.7) is the shot noise contribution from the random distribution of halos on the sky. This contribution can be expressed as (Lidz et al. 2011)

$$P_{\text{shot}}(z) = \frac{1}{f_{\text{duty}}} \frac{\langle M^2 \rangle}{\langle M \rangle^2}, \quad (2.17)$$

where

$$\langle M^2 \rangle = \int_{M_{\text{CO},\text{min}}}^{\infty} M^2 \frac{dn}{dM} dM, \quad (2.18)$$

and

$$\langle M \rangle = \int_{M_{\text{CO},\text{min}}}^{\infty} M \frac{dn}{dM} dM. \quad (2.19)$$

Note that the shot noise has no dependence on wavenumber.

The above expressions give the 3D power spectrum for CO emission. However, especially for the initial measurements of this signal, it is more natural to consider the angular power spectrum projected on the sky. The exact expression for converting a spatial power spectrum $P(k)$ to an angular spectrum C_ℓ is

$$C_\ell = \frac{2}{\pi} \int k^2 P(k) \left[\int f(r) j_\ell(kr) dr \right]^2 dk, \quad (2.20)$$

where r is the comoving distance, $j_\ell(kr)$ is the spherical bessel function and $f(r)$ is the frequency function which is determined by the frequency bandwidth of the instrument

used to observe the CO emission. For simplicity, we use a top hat $f(r)$ for this analysis.

Equation (2.12) is somewhat time consuming to evaluate numerically, so we take steps to simplify the calculation somewhat. One method commonly referred to as the Limber approximation (Limber 1953; Rubin 1954) is obtained by assuming the power spectrum is a slowly varying function of k

$$C_\ell = \int \frac{H(z)}{c} \frac{f^2(z)}{r^2(z)} P_{\text{CO}}[k = \ell/r(z), z] dz. \quad (2.21)$$

However, this approximation is only valid when the width δr of the selection function satisfies $\ell \delta r/r \gg 1$, i.e. when the width of the observed shell is large compared to the scale of fluctuations being considered. For small ℓ 's and small frequency bandwidths the Limber approximation fails. In the regime where $\ell \delta r/r \ll 1$, we can instead simplify the calculation by approximating $f(r)$ as a delta function. The angular power spectrum for a selection function centered on redshift z_0 is then given by

$$C_\ell = \frac{2}{\pi} \int k^2 P(k) j_\ell^2[kr(z_0)] dk. \quad (2.22)$$

Some attempts have been made to simplify this expression further by assuming $P(k)$ is a power law (Zaldarriaga, Furlanetto, & Hernquist 2004), but that approximation only works if the slope of the power law is less than 2. Since the slope of $P_{\text{CO}}(k)$ is near 3 in the range of interest, we cannot use this approximation.

We calculate the full angular power spectrum by using equations (2.21) and (2.22) in the areas where they are valid and interpolating between them. Figure 1 shows the clustering (solid lines) and shot noise (dashed lines) terms of the angular power spectrum for our fiducial model P13A for instruments with different bandwidths. These power spectra are calculated at $z = 3$. As the bandwidth increases, the amplitude of the signal falls off sharply. This makes it very difficult to find this signal in WMAP or Planck data since those instruments had very wide frequency bands. This is likely why the attempt in P13 to find the CO signal in WMAP data was unsuccessful. Also note that at small bandwidths, the clustering term approaches a maximum amplitude. This is due to the use of equation (2.22) at low ℓ 's. If only the Limber approximation was used, the clustering term would continue to increase beyond the limit seen here. Figure 2 shows this effect for the two narrowest bandwidths from Figure 1.

3 SIGNAL-TO-NOISE ESTIMATION

We now introduce a sample instrument to measure the CO signal and estimate the signal-to-noise ratio it would produce. We consider a spectrograph with a 1 GHz total bandwidth targeted at $z = 3$. This bandwidth is split into 35 channels, giving a spectral resolution $R = 1000$. We assume an observation time $t_{\text{obs}} = 1$ yr and choose the detector sensitivity s and beam size θ_{fwhm} to be $800 \mu\text{K}\sqrt{s}$ and 10 arcminutes respectively. These values are comparable to those for experiments currently under consideration (see, for example, Visbal, Trac, & Loeb (2011) and P13). For a survey

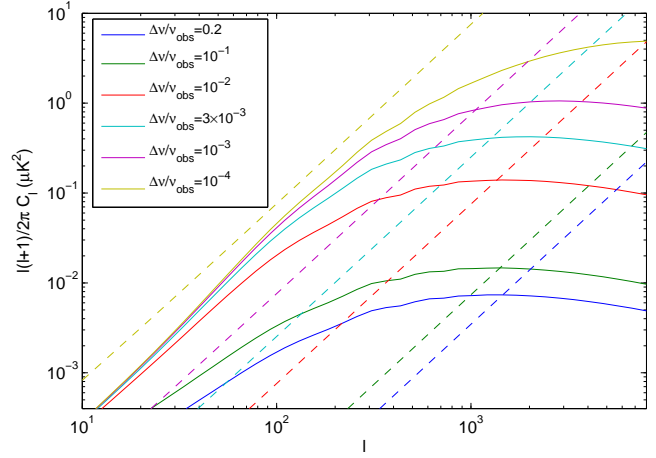


Figure 1. Clustering term of the angular CO power spectrum at $z_0 = 3$ for instruments with different frequency bandwidths. The solid lines show the contribution from the clustering term and the dashed lines show the contributions from shot noise. The clustering term loses its dependence on frequency bandwidth when the width of the spatial shell being observed becomes smaller than the size of the features being probed at a given ℓ value.

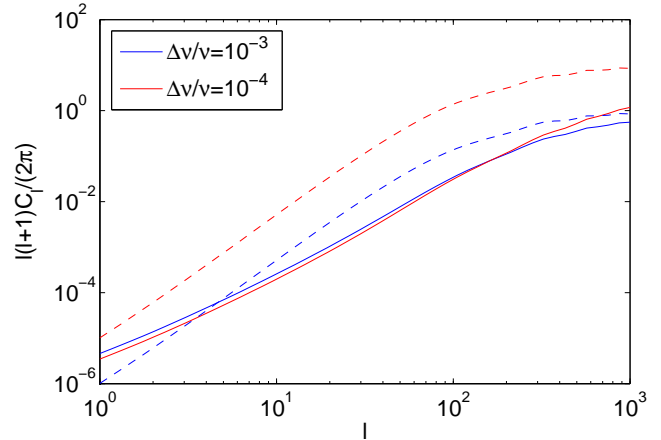


Figure 2. Comparison of full power spectrum (solid) with Limber approximation (dashed) for two narrow frequency bandwidths. The Limber approximation fails in this case because the width of the redshift shell being probed is small compared to the spatial size of the brightness fluctuations.

covering a solid angle Ω_s , the instrumental noise can be modeled as a random field on the sky with a power spectrum

$$C_\ell^m = \frac{s^2 \Omega_s}{t_{\text{obs}} B_\ell^2} \quad (3.1)$$

(Tegmark 1997), where B_ℓ is the beam profile, typically approximated as a Gaussian,

$$B_\ell = e^{-8 \ln(2) \theta_{\text{fwhm}}^2 \ell(\ell+1)/2}. \quad (3.2)$$

The angular power spectrum can be measured in each channel of this spectrograph, after which the signals can be stacked to increase the overall SNR. The SNR for such an instrument with N_{ch} channels is given by

$$\text{SNR}^2 = N_{ch} \sum_\ell \frac{C_\ell^2}{\sigma_\ell^2}. \quad (3.3)$$

where

$$\sigma_\ell = \sqrt{\frac{8\pi}{\Omega_s(2\ell+1)}} C_\ell^n, \quad (3.4)$$

(Jaffe, Kamionkowski, & Wang 2000). Combining equations (3.3) and (3.4) with equation (3.1) yields

$$SNR^2 = \frac{N_{ch}}{8\pi} \left(\frac{A}{A_{P13}} \right)^2 \frac{t_{obs}}{s^4 \Omega_s} \sum_\ell C_\ell^{P13A} e^{-16 \ln(2)\theta_{fwhm} \ell(\ell+1)}, \quad (3.5)$$

where C_ℓ^{P13A} is the angular power spectrum in the P13A model.

This expression is only valid if one is testing against the null hypothesis, i.e. if one is only interested in seeing if this signal exists at all. It is useful for a first detection attempt, but when trying to obtain useful cosmological information from a signal it is necessary to include an extra cosmic variance term in equation (3.4) to account for the limited number of modes available in the survey. The signal variance in this case is given by

$$\sigma_\ell = \sqrt{\frac{8\pi}{\Omega_s(2\ell+1)}} (C_\ell + C_\ell^n). \quad (3.6)$$

Under the null hypothesis, equation (3.5) clearly shows that a smaller, higher resolution survey will always give a higher SNR. If cosmic variance is included, surveys which are too small will yield smaller SNR's because they include fewer modes. These behaviors can clearly be seen in Figure 3, which shows how SNR depends on survey area and beam size, and Figure 4, which shows how SNR depends on area for our fiducial 10 arcmin beam. We choose our fiducial value of the survey area to be $\Omega_s = 9.8 \text{ deg}^2$ because this is the value which maximizes the SNR with cosmic variance included. This is a much smaller area than what was chosen for a similar spectrograph suggested in P13, but it has a much higher possible SNR since each pixel is studied more deeply.

Given the wide variation in the signals predicted by the four models we discussed above, we predict a wide range of possible SNR. Figure 5 shows the SNR as a function of the parameter A , with the values for the four models discussed above marked by dashed red lines. The curve for the null hypothesis is simply a power law since $SNR \propto A^2$ when cosmic variance is neglected. Possible values of SNR range from 5.8 (VL10) to 1390 (P13B) under the null hypothesis and from 5.2 (VL10) to 60 (P13B) including cosmic variance. All of the models except the most pessimistic have a good chance to detect the signal.

3.1 Survey Parameters

As shown in Figure 3 above, the parameters of an intensity mapping survey must be carefully chosen to maximize the chance to detect the signal. Here we explore the dependence of SNR on some of the other survey parameters. The first possibility we consider is altering the redshift targeted by the survey to see if $z = 3$ is actually the best redshift to target. Figure 6 shows the SNR as a function of the central redshift of the survey for our optimal spectrograph. It is clear that SNR can be increased by targeting lower redshifts

The SNR actually peaks at redshifts slightly higher than 3 with cosmic variance included, but the additional SNR

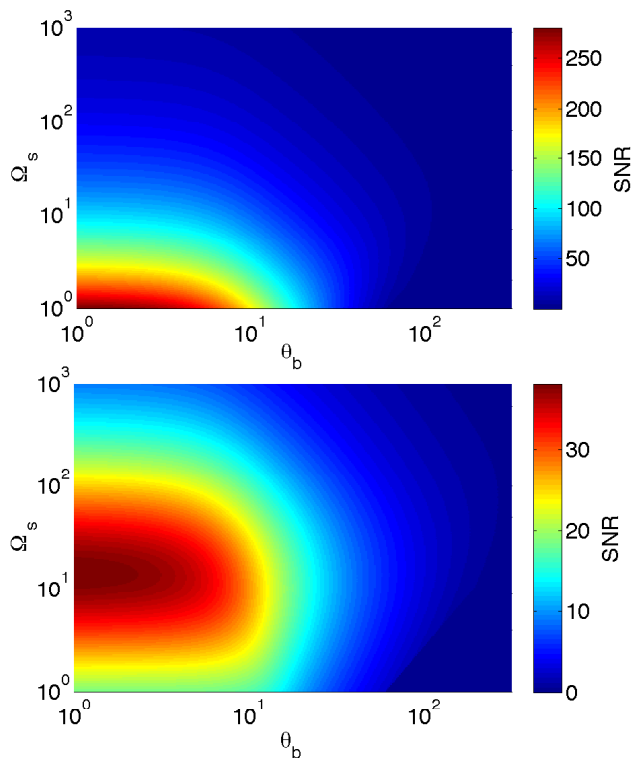


Figure 3. SNR as a function of beam size and survey area for our hypothetical spectrograph in the null hypothesis (top panel) and including cosmic variance (bottom panel). A smaller, higher-resolution survey will always improve the chances of a simple detection, but surveys which are too small lose cosmological information because they include fewer modes.

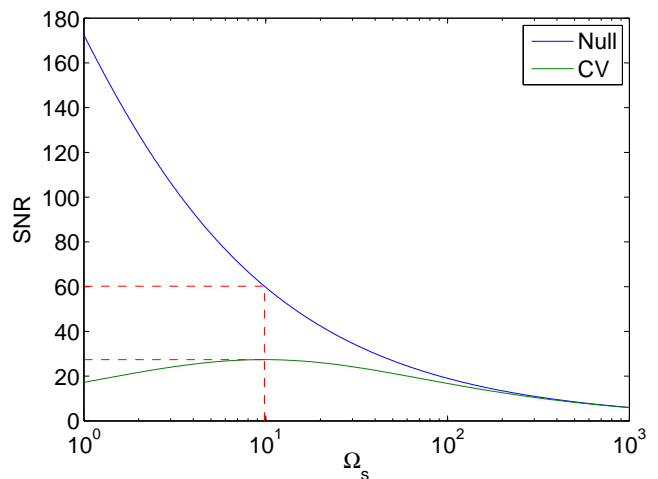


Figure 4. SNR as a function of survey area with a beam size of 10 arcmin with and without cosmic variance. The same behaviors seen in Figure 3 are visible here as well.

gained from increasing the redshift is minor. The null hypothesis gives higher SNR's a lower redshifts, but since the cosmic variance SNR drops off at lower redshifts $z = 3$ appears to be a good place to target.

Figure 7 shows the effect of varying the number of frequency channels in the spectrographs. The total 1 GHz bandwidth is held constant, so if N_{ch} is increased the

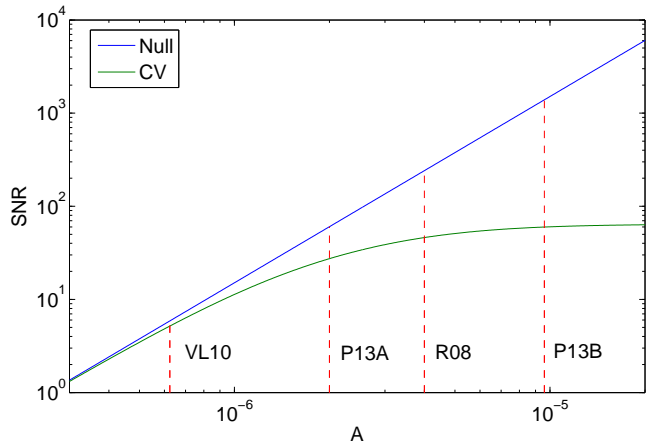


Figure 5. signal-to-noise ratio as a function of parameter A for our hypothetical spectrograph with and without cosmic variance. Values for the four models discussed above are marked.

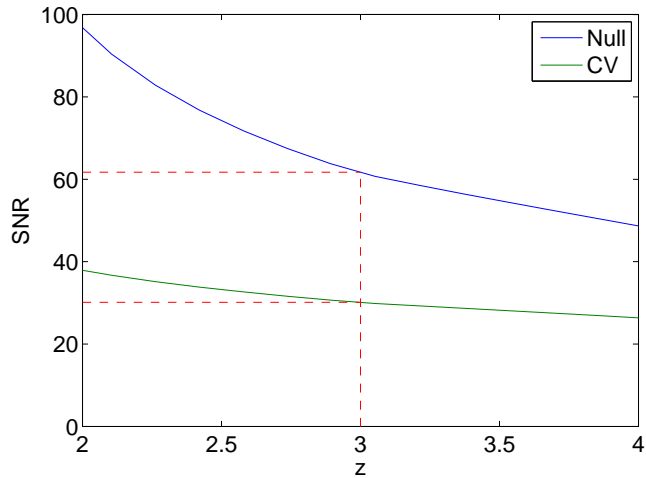


Figure 6. signal-to-noise ratio as a function of central redshift for our hypothetical spectrograph with and without the null hypothesis, with the value at $z = 3$ marked. The total bandwidth of the spectrograph is held constant at 1 GHz while the central frequency is varied.

width of an individual channel is decreased. The proposed $N_{ch} = 35$ spectrograph has $\delta\nu/\nu_{obs} = 1 \times 10^{-3}$, so it can be seen from Figure 1 that there is little additional signal gained in the range of ℓ 's to which we are sensitive. In addition, the telescope sensitivity s is proportional to $\Delta\nu^{-1/2}$ (Visbal, Trac, & Loeb 2011) so the amplitude of the noise power spectrum increases for spectrographs with smaller channels. This is why the curves in Figure 7 flatten out for narrower channels. However, since a higher resolution spectrograph stacks signals from more channels, modest gains in SNR can still be obtained by using more channels.

Another obvious way to improve the SNR of a survey is simply to increase the total observation time. How much SNR can be gained by observing for longer periods is less obvious. Longer observing times decrease the amplitude of the noise power spectrum, but eventually the C_ℓ cosmic variance term in equation (3.6) starts to dominate over the C_ℓ^n term. At this point, it is more useful to survey a larger area of

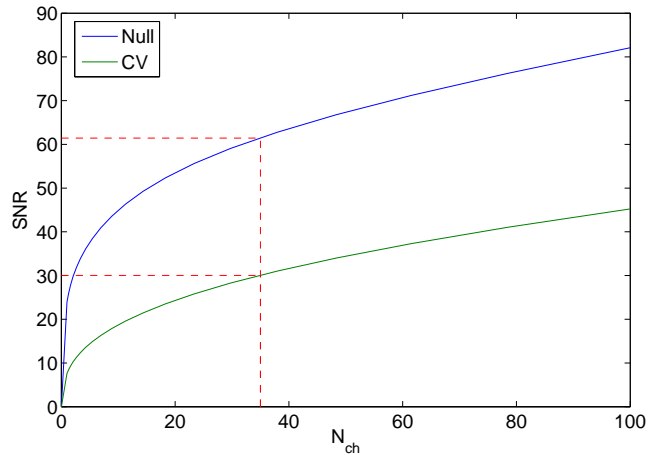


Figure 7. Signal to noise as a function of number of spectrograph channels with and without cosmic variance. The fiducial value $N_{ch} = 35$ is marked. The SNR shown here is obtained by stacking the signals from each of the N_{ch} channels.

sky rather than spend additional time on an already deeply studied patch. This effect is illustrated in figure 8, which shows the SNR as a function of survey area and observing time for our two spectrographs, assuming the values calculated above are for a 1 year survey. For longer observations, the maximum SNR is obtained by surveying a larger area of the sky.

4 CONCLUSION

We have presented a study based on several models of CO emission and a construction of an optimal survey aimed at detecting it. We briefly discussed four models which estimated the intensity of CO emission using slightly different methods and we found that the large theoretical uncertainties in the calculation lead to a broad range of possible values. When calculating signal-to-noise ratios for a representative of these models, model P13A, we found that the optimal survey to detect this signal is one which deeply surveys a relatively small portion of the sky. We found that the exact target redshift is not too important, and that an instrument with a higher spectral resolution can gain a slight increase in SNR. The instruments we describe here are able to attain a reasonable SNR given model P13A, and they could provide a much stronger detection considering either model R08 or P13B. Model VL10 is much more pessimistic, but since it is the most simplistic of the models (relying only on one galaxy for normalization), it appears less likely than the others.

It is important to note that all of our calculations in this paper have taken into account only instrumental noise and cosmic variance. We have not included any estimates of the impact of foregrounds on the signal-to-noise ratios above. Since we are looking at line emission, foregrounds with continuous spectra should be fairly easy to remove (Visbal, Trac, & Loeb 2011). However, it is possible for other lines besides the CO line we want to study to be redshifted into the same frequency range. This line confusion could be mitigated by cross-correlating the CO signal with another map of the same area, either another intensity map

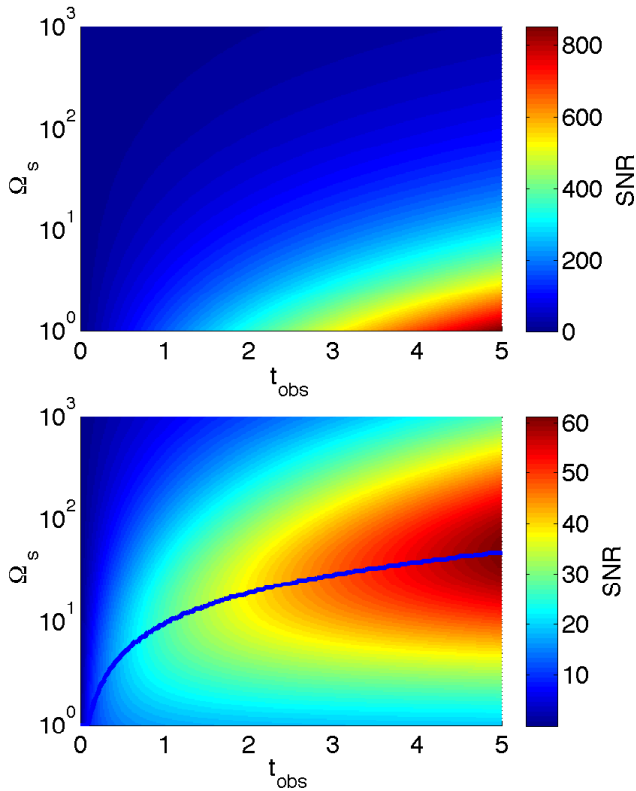


Figure 8. Signal to noise as a function of survey time and area for the null hypothesis (top panel) and including cosmic variance (bottom panel). The blue line in the bottom panel shows the optimal survey area for a given observing time assuming a 10 arcminute beam.

in a different frequency or a more traditional map of galaxies or quasars. Estimating the importance of line confusion is left for future study.

The results of this work suggest that it is possible to design a survey to detect the CO auto power spectrum if foregrounds are not a major concern. However, we have shown that the parameters of such a survey should be considered carefully in order to maximize the chance of detection. Analyses like this will be important if intensity mapping surveys are to reach their full potential.

This work was supported at Johns Hopkins by NSF Grant No. 0244990 and by the John Templeton Foundation. EDK was supported by the National Science Foundation under Grant Number PHY-1316033.

REFERENCES

- Adelman-McCarthy J. K., et al., 2008, *ApJS*, 175, 297
 Carilli C. L., 2011, *ApJ*, 730, L30
 Furlanetto S. R., Oh S. P., Briggs F. H., 2006, *PhR*, 433, 181
 Gong Y., Cooray A., Silva M., Santos M. G., Bock J., Bradford C. M., Zemcov M., 2012, *ApJ*, 745, 49
 Hinshaw G., et al., 2013, *ApJS*, 208, 19
 Hopkins A. M., Beacom J. F. 2006, *ApJ*, 651, 142
 Jaffe A. H., Kamionkowski M., Wang L., 2000, *PhRvD*, 61, 083501

- Lidz A., Furlanetto S. R., Oh S. P., Aguirre J., Chang T.-C., Doré O., Pritchard J. R., 2011, *ApJ*, 741, 70
 Limber D. N., 1953, *ApJ*, 117, 134
 Loverde M., Afshordi N., 2008, *PhRvD*, 78, 123506
 Mo H. J., White S. D. M., 2002, *MNRAS*, 336, 112
 Muñoz J. A., Furlanetto S. R., 2013, *MNRAS*, 435, 2676
 Planck Collaboration, et al., 2013, *arXiv*, arXiv:1303.5062
 Pullen A. R., Chang T.-C., Doré O., Lidz A., 2013, *ApJ*, 768, 15
 Pullen A., Dore O., Bock J., 2013, *arXiv*, arXiv:1309.2295
 Righi M., Hernández-Monteagudo C., Sunyaev R. A., 2008, *A&A*, 489, 489
 Rubin V. C., 1954, *PNAS*, 40, 541
 Schechter P., 1976, *ApJ*, 203, 297
 Sheth R. K., Mo H. J., Tormen G., 2001, *MNRAS*, 323, 1
 Suginozawa M., Suginozawa T., Spergel D. N., 1999, *ApJ*, 512, 547
 Tegmark M., 1997, *PhRvD*, 56, 4514
 Tinker J., Kravtsov A. V., Klypin A., Abazajian K., Warren M., Yepes G., Gottlöber S., Holz D. E., 2008, *ApJ*, 688, 709
 Visbal E., Loeb A., 2010, *JCAP*, 11, 16
 Visbal E., Trac H., Loeb A., 2011, *JCAP*, 8, 10
 Weiß A., Walter F., Scoville N. Z., 2005, *A&A*, 438, 533
 Zaldarriaga M., Furlanetto S. R., Hernquist L., 2004, *ApJ*, 608, 622